

MULTI EPOCH SPATIALLY RESOLVED RADIO OBSERVATIONS OF BETELGEUSE’S WIND ACCELERATION REGION

EAMON O’GORMAN¹, GRAHAM M. HARPER¹, ALEXANDER BROWN², AND ANITA M. S. RICHARDS³

Draft version July 11, 2014

ABSTRACT

We present multi-epoch spatially resolved radio continuum observations of Betelgeuse at various combinations of wavelengths between 0.7 – 20.5 cm. We used the Very Large Array (VLA) in the A configuration with the Pie Town (PT) Very Long Baseline Array (VLBA) antenna to fully resolved its atmosphere at 0.7, 1.3, 2.0, and 6.0 cm at all epochs, and provide flux measurements at 20.5 cm. Our low-frequency observations confirm the multiple outburst interpretation of the spectral index differences at high frequencies.

New multi-epoch e-MERLIN data are urgently required. Betelgeuse’s inner atmosphere has undergone a major morphological change in the past 10 years.

Keywords: Radio continuum: stars — Stars: supergiants — Stars: individual (α Ori) — Stars: mass-loss — Stars: winds, outflows

1. INTRODUCTION

Red supergiants (RSGs) lose mass to the interstellar medium in the form of a massive ($\dot{M} \sim 10^{-7} - 10^{-4} M_{\odot} \text{ yr}^{-1}$) cool wind, with terminal velocities ($10 \lesssim v_{\infty} \lesssim 50 \text{ km s}^{-1}$) typically less than the photospheric escape velocity ($v_{\text{esc}} \sim 100 \text{ km s}^{-1}$). These winds are major contributors of heavy elements to the interstellar medium (ISM) and play a crucial role in stellar evolution (Chiosi & Maeder 1986), and also in explaining the frequency of supernovae in the galaxy (e.g., van Loon 2010). Despite their importance, the mechanisms responsible for the formation of these winds in late K and early M-type RSGs remain largely unknown. Dust is observed too far from the star to play a significant role in the mass-loss process (Danchi et al. 1994) and pulsation amplitudes are too low to initiate the mass-loss (Smith et al. 1989). Magnetohydrodynamic (MHD) waves (e.g., Thirumalai & Heyl 2012) and large convective cells (e.g., Josselin & Plez 2007) have been proposed as alternative potential mass-loss mechanisms in RSGs but spatially resolved multi-epoch observations of RSGs are required to test these competing theories.

1.1. Tracing Betelgeuse’s Mass Loss History

Betelgeuse (α Ori, M2Iab) is the closest isolated RSG ($d = 197 \pm 45 \text{ pc}$; Harper et al. 2008) and is therefore the prototype of the late K and early M spectral type RSG class. Its large angular diameter ($\phi_{\star} = 42.49 \pm 0.06 \text{ mas}$ in the K band, Ohnaka et al. 2011) coupled with its extended atmosphere makes it an excellent target for detailed multi-wavelength studies aiming to build a complete understanding of mass-loss in RSGs. Such studies have recently been carried out and have traced the ejected material over various spatial scales between the ISM and the photosphere. The wind-ISM interaction produces a multi-arc bow shock structure (Decin et al.

2012) and a detached HI shell elongated in the south-west direction (Le Bertre et al. 2012). Two distinct flows in its circumstellar envelope (CSE) were imaged at 1.3 mm by O’Gorman et al. (2012) which traced CO($J = 2 - 1$) on scales between $\sim 40 R_{\star}$ and $\sim 750 R_{\star}$. These observations revealed an irregular CSE with a notable asymmetry in the south-west direction extending out to $\sim 200 R_{\star}$. Thermal infrared images using the Very Large Telescope (VLT) uncovered an envelope of inhomogeneous surface brightness up to $100 R_{\star}$, whose spectral energy distribution is typical of oxygen-rich dust (Kervella et al. 2011). These images also uncovered a ring-like structure at radius $20 - 45 R_{\star}$ which may be related to the dust condensation radius. The inner CSE was probed in the near-infrared with the VLT by Kervella et al. (2009) who discovered a molecular plume extending out to almost $6 R_{\star}$ in the south-west direction, which they attributed to the action of a photospheric giant convective cell. Indeed, the photospheric bright spots detected on Betelgeuse by Haubois et al. (2009) have now been attributed to presence of giant convective cells (Chiavassa et al. 2010). However, this does not provide definitive evidence that such convective cells are actually responsible for initiating the mass-loss.

1.2. Betelgeuse at Centimeter Wavelengths

Thermal free-free centimeter continuum emission directly probes the chromospheres and wind acceleration regions of RSGs; the regions identified as the most important for studies of mass-loss mechanisms in evolved stars (Holzer & MacGregor 1985). The first detailed study of Betelgeuse at centimeter wavelengths was carried out with the Very Large Array (VLA) by Newell & Hjellming (1982). The source was unresolved but the radio emission was interpreted as chromospheric in origin and extending from $1 - 4 R_{\star}$. This was in agreement with the Alfvén wave models to follow (Hartmann & Avrett 1984) and later Hubble Space Telescope (*HST*) spatially resolved ultraviolet observations (Gilliland & Dupree 1996; Uitenbroek et al. 1998). Spatially resolved VLA plus Multi-Element Radio Linked Interferometer Network (MERLIN) observations at 6 cm also confirmed the extended

¹ School of Physics, Trinity College Dublin, Dublin 2, Ireland

² Center for Astrophysics and Space Astronomy, University of Colorado, 389 UCB, Boulder, CO 80309, USA

³ Jodrell Bank Centre for Astrophysics, School of Physics and Astronomy, University of Manchester, Manchester M13 9PL, UK

nature of the radio emitting region (Skinner et al. 1997).

Lim et al. (1998) used the VLA in its most extended (i.e., A) configuration to resolve Betelgeuse’s atmosphere at 0.7 cm and partially resolve it at 1.3, 2.0, 3.6, and 6 cm. Because the radio emission is thermal and optically thick, they were able to calculate the mean gas temperature as a function of radius and discovered that the mean gas temperature never reached chromospheric values (i.e., $\gtrsim 5000$ K) but decreased steadily from ~ 3450 K at $2 R_\star$, to ~ 1370 K at $7 R_\star$. They also detected an asymmetry in their 0.7 cm image which they attributed to the action of a large convective cell. To reconcile their results with the extended ultraviolet observations, which probed the same regions, they concluded that the inner atmosphere must be inhomogeneous to accommodate the hot chromospheric plasma, but that the cooler gas must be 3 orders of magnitude more abundant. Harper & Brown (2006) used observations of the chromospheric tracer C II] $\lambda 2325$ Å to confirm this low filling factor for the chromospheric gas.

Recently, an unexpected new discovery by Richards et al. (2013) with e-MERLIN, has revealed that two unresolved radio features dominate the total flux density at 5.2 cm. The two “radio hotspots” are separated by 90 ± 10 mas (i.e., $\sim 4 R_\star$) and have gas temperatures $T_e \geq 3800 \pm 500$ K and $T_e \geq 5400 \pm 600$ K, with the later value significantly above the photospheric temperature ($T_{\text{eff}} = 3690 \pm 54$ K, Ohnaka et al. 2011). The features are so extended that they presumably have either momentum or support and are probably connected with the mass-loss mechanism in Betelgeuse. The potential importance of these radio hotspots has been the motivation for this paper. In the following sections we present, analyze, and discuss multi-epoch, multi-wavelength radio observations of Betelgeuse, taken ~ 10 years prior to the e-MERLIN observations. At short wavelengths, our data has comparable or superior resolution to the e-MERLIN data and so the goal of the paper is to search for signatures of these features to improve our understanding of Betelgeuse’s wind acceleration region.

2. OBSERVATIONS AND DATA REDUCTION

Betelgeuse was observed with the NRAO⁴ VLA in the A configuration with the Pie Town (PT) Very Long Baseline Array (VLBA) antenna at multiple epochs between December 2000 and October 2004. The PT antenna is located 50 km from the center of the VLA, and its inclusion to the A configuration enhances the east-west resolution by a factor of 2. Our observations are summarized in the first two columns of Table 1. Our two multi-wavelength data sets in 2002 (Program: AH0778) were taken only ~ 2 months apart and consist of all wavelength bands between 1.3 and 20.5 cm. We observed the star again under program AH0824 in 2003 and 2004 at all wavelength bands between 0.7 and 20.5 cm. We also obtained VLA A configuration plus PT antenna data from the NRAO data archive (Program: AL0525) at 0.7 and 1.3 cm which were taken in late 2000 and early 2001, respectively.

We used the “fast switching” phase calibration technique at 0.7 and 1.3 cm to compensate for tropospheric

phase variations. This allowed us to switch between observations of the point source phase calibrator 0532+075 and Betelgeuse, with cycle times of 2 – 3 min at 0.7, 1.3 and 2.0 cm. The archival data from 2000/2001 also implemented the fast switching technique at these wavelengths but used the point source phase calibrator 0552+032, which was ~ 10 times more faint at 0.7 cm but 1.4° closer to Betelgeuse. We again used interleaving observations of 0532+075 to calibrate phase variations at longer wavelengths, but implemented longer cycle times of 10 – 20 min. Absolute flux calibration was obtained from 3C 48 at 6.1 cm, and 3C 286 at all other wavelengths. The absolute flux density uncertainty is estimated to range from 5% to 10% between the longest to shortest wavelengths, respectively. The flux density error values quoted in the remainder of this paper do not include this systematic error but represent the $\pm 1\sigma$ value. The raw visibilities were flagged and calibrated according to standard VLA continuum data reduction procedures using the Astronomical Image Processing System (AIPS; Greisen 1990). The calibrated visibilities were imaged in both AIPS and the Common Astronomical Software Application (CASA; McMullin et al. 2007) package.

2.1. Imaging

The calibrated visibilities at all wavelengths were imaged using CASA’s *clean* task while applying uniform weighting. With uniform weighting, each visibility is given a weight that is inversely proportional to the sampling density function. This optimises the full resolution of the array and minimises the sidelobe level. However, it also leads to an increase in the image noise level in comparison to natural weighting, which gives a constant weight to all visibilities, and Briggs weighting, which is a compromise between uniform and natural weighting. Additional images were also created at 0.7 and 1.3 cm which implemented both Briggs weighting, and natural weighting with a restoring beam size equal to that obtained using uniform weighting, as used in Lim et al. (1998). These additional images were used to check if asymmetries produced by one weighting scheme could be reproduced by another.

2.2. Calibrated Visibilities

Betelgeuse’s position was initially offset by a few restoring beams from the interferometer phase center to avoid any possible spurious artefacts which might accumulate there. One such artefact was noticed in the 2.0 cm image from April 2002 but our target was sufficiently far away and was not contaminated. We fitted elliptical Gaussian brightness distributions to the source at each wavelength and epoch and measured the position of the peak emission. We then used CASA’s *fixvis* task to shift the visibilities such that this peak emission position was placed at phase center. The Python-based task *uvmultifit* (Martí-Vidal et al. 2014) was then used to fit elliptical disks to the calibrated visibilities, with the major axis (θ_{maj}), axis ratio ($\theta_{\text{min}}/\theta_{\text{maj}}$, where θ_{min} is the minor axis), position angle (P.A.), and flux density (F_ν) left as free parameters. We bounded the axis ratio between 0 and 1, and the position angle between 0 and 180° .

3. RESULTS

⁴ The National Radio Astronomy Observatory is a facility of the National Science Foundation operated under cooperative agreement by Associated Universities, Inc.

Table 1
Multi Epoch VLA A Configuration Plus PT Link Observations of Betelgeuse.

Date	Wavelength (cm)	Restoring Beam (mas × mas)	Image rms (mJy/Beam)	θ_{maj} (mas)	θ_{min} (mas)	P.A. (deg)	F_{ν} (mJy)	T_b (K)
2004 Oct 21,30	0.7	39 × 26	0.37	99 ± 3	92 ± 3	92 ± 20	28.68 ± 0.53	2940 ± 170
	1.3	80 × 42	0.09	127 ± 2	114 ± 2	85 ± 5	13.83 ± 0.10	3140 ± 80
	2.0	121 × 91	0.08	158 ± 6	152 ± 10	132 ± 59	7.23 ± 0.15	2270 ± 130
	3.6	208 × 126	0.02	215 ± 7	188 ± 7	0 ± 10	3.34 ± 0.03	2110 ± 110
	6.1	377 × 264	0.02	314 ± 30	203 ± 30	0 ± 20	1.55 ± 0.04	1140 ± 160
	20.5	1262 × 889	0.03	< 889	< 889	...	0.25 ± 0.03	>260
2003 Aug 10,12	0.7	40 × 27	0.46	103 ± 4	92 ± 5	104 ± 16	28.05 ± 0.84	2760 ± 230
	1.3	80 × 42	0.17	122 ± 5	114 ± 6	0 ± 5	11.20 ± 0.24	2490 ± 150
	2.0	119 × 96	0.10	132 ± 10	116 ± 9	11 ± 27	5.88 ± 0.17	3040 ± 360
	3.6	204 × 139	0.03	193 ± 7	140 ± 11	152 ± 7	2.80 ± 0.04	2610 ± 170
	6.1	378 × 297	0.03	247 ± 47	179 ± 61	169 ± 28	1.22 ± 0.04	2040 ± 680
	20.5	1247 × 931	0.04	< 931	< 931	...	0.26 ± 0.03	>250
2002 Apr 12,13	1.3	91 × 59	0.18	134 ± 9	102 ± 6	36 ± 10	8.96 ± 0.24	2170 ± 250
	2.0	131 × 98	0.39	166 ± 16	104 ± 13	41 ± 11	5.32 ± 0.24	2420 ± 450
	3.6	224 × 155	0.03	234 ± 9	171 ± 10	41 ± 7	2.66 ± 0.04	1690 ± 110
	20.5	1398 × 1146	0.06	< 1146	< 1146	...	0.38 ± 0.06	>240
2002 Feb 17,18	1.3	83 × 48	0.14	120 ± 4	109 ± 3	31 ± 13	10.87 ± 0.17	2750 ± 140
	2.0	128 × 90	0.11	140 ± 13	135 ± 16	0 ± 28	5.38 ± 0.22	2150 ± 300
	3.6	200 × 135	0.03	217 ± 9	183 ± 10	0 ± 5	2.85 ± 0.04	1830 ± 110
	20.5	1312 × 951	0.05	< 951	< 951	...	0.30 ± 0.05	>270
2001 Jan 02	1.3	78 × 42	0.08	124 ± 2	115 ± 1	40 ± 8	12.58 ± 0.08	2920 ± 70
2000 Dec 23	0.7	44 × 20	0.18	98 ± 2	91 ± 1	0 ± 8	29.02 ± 0.30	3070 ± 100

Notes.- The restoring beam sizes and image rms noise values are taken from the uniformly weighted radio maps that include the PT antenna baselines. The position angles (measured in degrees east of north) of the restoring beams are not quoted here, but are all between 30° and 70°. The major and minor axis of the stellar radio disk θ_{maj} and θ_{min} , the position angle P.A., and the total flux density F_{ν} , are all derived from the best-fit uniform-brightness (T_b) elliptical-disk models. The atmosphere at 20.5 cm was unresolved so we define the minor axis of the restoring beam as the upper limit to its diameter.

3.1. Radio Maps

Radio maps were produced at all wavelengths using uniform weighting to utilize the full capabilities of the PT baselines and achieve maximum spatial resolution. The corresponding restoring beam sizes and image rms noise levels are provided in columns 3 and 4 of Table 1. Calibrations issues with the two 6.1 cm data sets from 2002 resulted in rms noise values being 10 times higher than expected. This resulted in the source not being detected in the April 2002 map and the source being located ~ 300 mas away from its expected position in the February 2002 map. We therefore do not include these 6.1 cm results in Table 1 and in any of the analysis. The remainder of the maps were generally of excellent quality with the source clearly resolved at the shorter wavelengths. No significant deviations from π -rotational symmetry were present in any of the maps between 1.3 and 20.5 cm and no ‘radio hotspots’ were present.

All of the 0.7 cm maps showed significant deviations from π -rotational symmetry. However, when these data sets were imaged using the different weighting schemes described in Section 2.1, the morphology was inconsistent. For example, the maps created using standard uniform weighing were morphologically different to the maps created using natural weighting with a restoring beam of size corresponding to that obtained with uniform weighting. These inconsistencies are probably due to poor phase stability resulting from rapid tropospheric phase fluctuations of which our cycle times were not short enough to compensate for. To investigate this further, we removed the PT antenna baselines and again imaged the data using the two aforementioned imaging techniques. We found that two data sets (i.e., from 2000 and 2004) produced images that had consistent morphology when

any of the imaging techniques were applied. The observing logs of the other data sets report poorer weather conditions in agreement with our imaging analysis. The resulting images are plotted in Figure 1 along with the 0.7 cm image from Lim et al. (1998) for comparison. In these data sets, the cycle time was adequate to obtain reasonable phase transfer from the calibrator to the source but shorter cycle times were probably required for the other data sets due to poorer weather. Unlike the Lim et al. (1998) map, no asymmetries are present in either of our two maps as is clearly evident in Figure 1. These maps indicate that large scale asymmetries are not always present in Betelgeuse’s inner atmosphere.

3.2. Radio Diameters

It can be seen in Figure 1 that the size of the source at 0.7 cm is only a few beam diameters across. The source to beam ratio gets progressively smaller at longer wavelengths which makes fitting models to the images unreliable. In this case it is best to obtain estimates of the source size and flux density by fitting models directly to the calibrated complex visibilities. In Figure 2 we plot the real component of the complex visibility against the projected baseline length in wavelengths, B_{λ} , for the 2004 epoch at all wavelengths between 0.7 – 6.1 cm. The data has been azimuthally vector averaged into uniformly sized bins over large portions of the unevenly sampled $u-v$ plane, where u and v are the spatial coordinates of the projected baseline in wavelengths, and $B_{\lambda} = \sqrt{u^2 + v^2}$. It is clear that the source is fully resolved at all wavelengths shown, i.e., we have obtained visibilities close to the first null. The VLA observations of Lim et al. (1998) only fully resolved Betelgeuse’s atmosphere at 0.7 cm at one epoch, but here we fully resolve

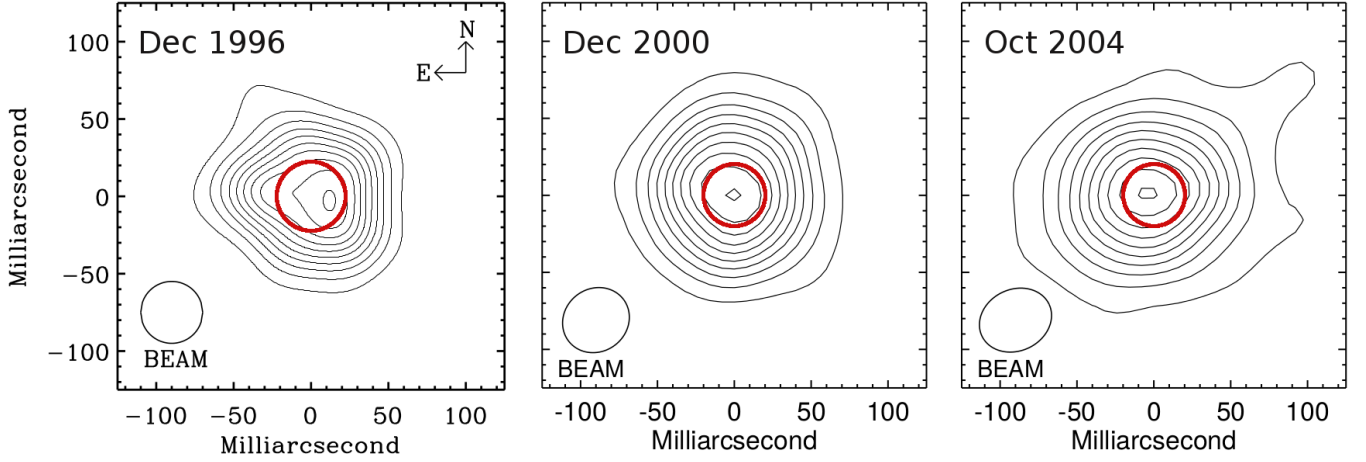


Figure 1. VLA A configuration maps of Betelgeuse at 0.7 cm over three different epochs. These maps have been created by naturally weighting the visibilities and applying a restoring beam corresponding to the size obtained from uniform weighting. The restoring beam size and shape is located in the bottom left corner of each panel while the red circle is the approximate location and size of the optical photosphere. The contour levels are plotted at 10%, 20%, ..., 90%, and 99% of the peak flux. From left to right the beam sizes are $40'' \times 40''$, $45'' \times 41''$, and $48'' \times 40''$, and the rms noise values are \times , 0.18, and $0.34 \text{ mJy beam}^{-1}$. *Left panel:* The Lim et al. (1998) map shows an asymmetry in the east direction. The position of the photosphere is here assumed to be *Middle and right panels:* Our maps show no significant deviations from the shape of the restoring beam. The position of the photosphere is here assumed to be located on the peak emission.

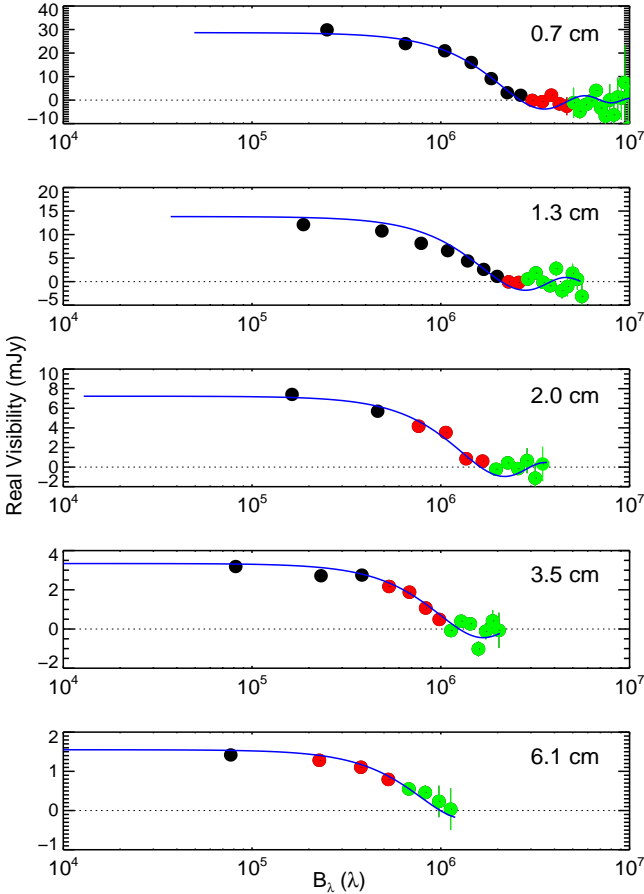


Figure 2. Real component of the complex visibility plotted against the projected baseline length in wavelengths, B_λ , for the 2004 epoch at all wavelengths between 0.7 – 6.1 cm. The black data point contain only VLA antenna baselines, the red data points contain both VLA and PT antenna baselines, while the green data points contain only PT antenna baselines. The solid blue line represents the theoretical visibilities of a uniform intensity circular disk with an *effective radius* defined as $\phi_{\text{eff}} = 0.5\sqrt{\theta_{\text{maj}}\theta_{\text{min}}}$.

the star at all wavelengths between 0.7 and 6.1 cm at all our epochs. The black data points in Figure 2 represent the real visibility measurements from the VLA antenna baselines only, the red data points include both VLA and PT antenna baselines, while the green data points include only PT antenna baselines. This highlights the importance of the inclusion of the PT antenna, especially at the longer wavelengths where it provides many baseline pairs close to the first null which helps to constrain the size of the extended atmosphere. The corresponding binned imaginary components of the complex visibility are not shown here but were mainly consistent with zero amplitude at all baselines, indicative of no significant asymmetrical structure.

Uniform intensity elliptical disk models were fitted to the complex visibilities as outlined in Section 2.2. The diameters and P.A.s of the best fits are listed in columns 5, 6, and 7 of Table 1. The source size is found to get progressively larger with increasing wavelength which implies that the radio surfaces are optically thick, in agreement with the findings of Lim et al. (1998). At 0.7 cm, these radio surfaces only slightly depart from spherical symmetry having axis ratios $\gtrsim 0.9$, in good agreement with the radio maps. This is also the case at 1.3 and 2.0 cm except in 2002 April where the axis ratios change to 0.76 ± 0.07 and 0.63 ± 0.10 respectively, from near spherical symmetric values two months prior. At 3.5 and 6.1 cm the radio surfaces display more consistent deviations from spherical symmetry having axis ratios ranging between 0.65 ± 0.10 and 0.87 ± 0.04 . The intrinsic beam is elongated at all wavelengths due to inclusion of the PT antenna so caution must be exercised when reporting deviations from spherical symmetry.

In Figure 2 we also plot the theoretical visibility curves of a uniform intensity circular disk with an *effective radius* defined as $\phi_{\text{eff}} = 0.5\sqrt{\theta_{\text{maj}}\theta_{\text{min}}}$. The scatter between these model curves and the azimuthally averaged real visibility is low and indicates that circular disks represent the radio surfaces well. This is found to be the

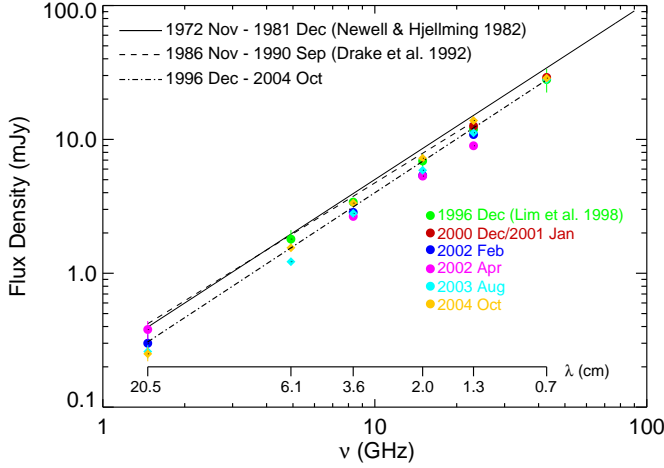


Figure 3. xxx

case at all epochs. Bearing in mind that the data is sparsely sampled between 2000 December and 2004 October we can cautiously investigate how the size of the atmosphere changes over this time frame. At 0.7 and 1.3 cm there is no significant change in ϕ_{eff} at all epochs with $\Delta\phi_{\text{eff}} \lesssim 3\%$ about the mean, i.e., there is no significant change in the size of the inner atmosphere. We see more variability at longer wavelengths which sample the more extended atmosphere with $\Delta\phi_{\text{eff}} \sim 14\%$ about the mean at 2.0 and 3.5 cm. In fact at these two wavelengths, ϕ_{eff} increases by $\sim 24\%$ in the 14 months between our 2003 and 2004 observations. We only have two measurements at 6.1 cm and these again show an increase in ϕ_{eff} between 2003 and 2004 with $\Delta\phi_{\text{eff}} = 20\%$, although the error are too large to be certain of this increase at 6.1 cm.

3.3. Flux Densities

obtained from visibility fits but also checked against elliptical Gaussian fitted results plot flux versus frequency (see harper paris presentation) $F_\nu = 0.185 \text{ mJy } \nu^{1.33}$

3.4. Temperature Profiles

give more exact lim formula

4. DISCUSSION

4.1. Radio Flux Density Variability

see Reid & Menton 1996 conf proceedings
see Drake conf proceedings
e-MERLIN flux is concentrated
see Harper variability. ps
does flux go up as ang diam go up
see Harper 2001 discussion

4.2. Structure of Wind Acceleration Region

Thermal structure (Lim vs vs Ours vs e-MERLIN)

see Reid & Menton 1996 conf proceedings

Harper model

Highlighted skinner discussion on velocities needed to produce a change in size

4.3. Where are the Hotspots?

No sign of hotspots (see Harpers pie town proceedings)
) See harper 2001 discussion emerlin rules out convective cells, magnetic fields?

5. CONCLUSIONS

The data presented in this paper were obtained with the Karl G. Jansky Very Large Array (VLA) which is an instrument of the National Radio Astronomy Observatory (NRAO). The NRAO is a facility of the National Science Foundation operated under cooperative agreement by Associated Universities, Inc.

Facilities: VLA.

REFERENCES

- Chiavassa, A., Haubois, X., Young, J. S., Plez, B., Josselin, E., Perrin, G., & Freytag, B. 2010, A&A, 515, A12
Chiosi, C., & Maeder, A. 1986, ARA&A, 24, 329
Danchi, W. C., Bester, M., Degiacomi, C. G., Greenhill, L. J., & Townes, C. H. 1994, AJ, 107, 1469
Decin, L., et al. 2012, A&A, 548, A113
Gilliland, R. L., & Dupree, A. K. 1996, ApJ, 463, L29
Greisen, E. W. 1990, in Acquisition, Processing and Archiving of Astronomical Images, ed. G. Longo & G. Sedmak, 125–142
Harper, G. M., & Brown, A. 2006, ApJ, 646, 1179
Harper, G. M., Brown, A., & Guinan, E. F. 2008, AJ, 135, 1430
Hartmann, L., & Avrett, E. H. 1984, ApJ, 284, 238
Haubois, X., et al. 2009, A&A, 508, 923
Holzer, T. E., & MacGregor, K. B. 1985, in Astrophysics and Space Science Library, Vol. 117, Mass Loss from Red Giants, ed. M. Morris & B. Zuckerman, 229–255
Josselin, E., & Plez, B. 2007, A&A, 469, 671
Kervella, P., Perrin, G., Chiavassa, A., Ridgway, S. T., Cami, J., Haubois, X., & Verhoelst, T. 2011, A&A, 531, A117
Kervella, P., Verhoelst, T., Ridgway, S. T., Perrin, G., Lacour, S., Cami, J., & Haubois, X. 2009, A&A, 504, 115
Le Bertre, T., Matthews, L. D., Gérard, E., & Libert, Y. 2012, MNRAS, 422, 3433
Lim, J., Carilli, C. L., White, S. M., Beasley, A. J., & Marson, R. G. 1998, Nature, 392, 575
Martí-Vidal, I., Vlemmings, W. H. T., Muller, S., & Casey, S. 2014, A&A, 563, A136
McMullin, J. P., Waters, B., Schiebel, D., Young, W., & Golap, K. 2007, in Astronomical Society of the Pacific Conference Series, Vol. 376, Astronomical Data Analysis Software and Systems XVI, ed. R. A. Shaw, F. Hill, & D. J. Bell, 127
Newell, R. T., & Hjellming, R. M. 1982, ApJ, 263, L85
O’Gorman, E., Harper, G. M., Brown, J. M., Brown, A., Redfield, S., Richter, M. J., & Requena-Torres, M. A. 2012, AJ, 144, 36
Ohnaka, K., et al. 2011, A&A, 529, A163
Richards, A. M. S., et al. 2013, MNRAS, 432, L61
Skinner, C. J., Dougherty, S. M., Meixner, M., Bode, M. F., Davis, R. J., Drake, S. A., Arens, J. F., & Jernigan, J. G. 1997, MNRAS, 288, 295
Smith, M. A., Patten, B. M., & Goldberg, L. 1989, AJ, 98, 2233
Thirumalai, A., & Heyl, J. S. 2012, MNRAS, 422, 1272
Uitenbroek, H., Dupree, A. K., & Gilliland, R. L. 1998, AJ, 116, 2501
van Loon, J. T. 2010, in Astronomical Society of the Pacific Conference Series, Vol. 425, Hot and Cool: Bridging Gaps in Massive Star Evolution, ed. C. Leitherer, P. D. Bennett, P. W. Morris, & J. T. Van Loon, 279